Retinal network characterization through fundus image processing: significant point identification on vessel centerline

S. Morales[a,b,*], V. Naranjo[a,b], J. Angulo[c], A.G. Legaz-Aparicio[d], R. Verdú-Monedero[d]

[a]*Instituto de Investigación e Innovación en Bioingeniería, I3B, Universitat Politècnica de València, Camino de Vera s/n, 46022, Valencia, Spain*
[b]*Grupo Tecnologías de Informática Aplicadas a la Oftalmología, Unidad Conjunta UPV-FISABIO, Spain*
[c]*MINES ParisTech, PSL-Research University, CMM-Centre de Morphologie Mathématique, France*
[d]*Universidad Politécnica de Cartagena, Cartagena, Spain*

Abstract

This paper describes a new approach for significant point identification on vessel centerline. Significant points such as bifurcations and crossovers are able to define and characterize the retinal vascular network. In particular, hit-or-miss transformation is used to detect terminal, bifurcation and simple crossing points but a post-processing stage is needed to identify complex intersections. This stage focuses on the idea that the intersection of two vessels creates a sort of close loop formed by the vessels and this effect can be used to differentiate a bifurcation from a crossover. Experimental results show quantitative improvements by increasing the number of true positives and reducing the false positives and negatives in the significant point detection when the proposed method is compared with another state-of-the-art work. A sensitivity equal to 1 and a predictive positive value of 0.908 was achieved in the analyzed cases. Hit-or-miss transformation must be applied on a binary skeleton image. Therefore, a method to extract the vessel skeleton in a direct way is also proposed. Although the identification of the significant points of the retinal tree can be

---

*Corresponding author
Email addresses:* `sanmomar@i3b.upv.es` (S. Morales), `vnaranjo@i3b.upv.com` (V. Naranjo)

useful by itself for multiple applications such as biometrics and image registration, this paper presents an algorithm that makes use of the significant points to measure the bifurcation angles of the retinal network which can be related to cardiovascular risk determination.

---

1. Introduction

Retinal structure characterization is a fundamental component of most automatic retinal disease screening systems [1]. It is usually a prerequisite previous to carrying out more complex tasks as identifying different pathologies. In general, anatomical structures are segmented through fundus image processing and then certain features are extracted from them to characterize each pathology. One of the most important anatomical structures of the fundus is the vascular network that corresponds to the retinal blood vessels. Morphological attributes of retinal blood vessels, such as length, width, tortuosity and/or branching pattern and angles can be used for diagnosis, screening, treatment, and evaluation of various cardiovascular and ophthalmologic diseases [2].

In the vessel centerline there are three types of significant points: terminal, bifurcation and crossing. The detection of significant points in the retinal vascular tree increases the information about the vascular structure allowing its use for medical diagnosis. In particular, the identification of the vascular bifurcations and crossovers on the vascular network is helpful for predicting cardiovascular diseases and can also be used as biometric features or for image registration [3].

This paper focuses on the identification of the significant points as a means of defining and characterizing the retinal vascular network. In general, the significant points of the vascular network are detected on vessel centerline, also called vessel skeleton. The centerline can be obtained after a skeletonization process of the vessels previously segmented or through some method by which

2

the skeleton is directly obtained. The main disadvantage of the first approach is that an inaccurate vessel segmentation may result in errors in the skeletonization. Motivated by that reason, this paper describes an approach to determine the retinal skeleton in a direct way through stochastic watershed transformation. Then, a new method to distinguish the different types of significant points on the retinal skeleton is presented. Finally, the proposed method is used as a necessary step before measuring bifurcation angles through the orientation vectors of each branch of the vascular tree.

In the literature there exist different attempts for significant point detection. Some of them are only based on bifurcation location [4] or on detecting bifurcations and the most simple intersections [5]. Other works take into consideration more types of crossovers since it is the most challenging part and try to distinguish between them and bifurcations. The most common approach is to center a fixed-size circular window on all bifurcations and check the number of intersections between the vessel centerline and the circular window [6, 7]. However, it causes that the large vessel crossovers are detected as two bifurcation points. Bhuiyan *et al.* addressed this problem by considering the width of the junction [3] and Calvo *et al.* by combining local and topological information [8].

Referring to vessel extraction techniques, they can be mainly divided into four categories: edge detectors, matched filters, pattern recognition techniques and morphological approaches. A more extensive classification can be found in [1]. Most edge detection algorithms assess changes between pixels values by calculating the image gradient magnitude and then it is thresholded to create a binary edge image [9, 10]. Matched filters are filters rotated in different directions in order to identify the cross section of blood vessels [11, 12]. Pattern recognition techniques can be divided into supervised and unsupervised approaches. Supervised methods, such as artificial neural networks [13] or support vector machines [14, 15], exploit some prior labelling information to decide whether a pixel belongs to a vessel or not, while unsupervised algorithms perform the vessel segmentation without any prior labelling knowledge [16]. Morphological processing is based on vessels characteristics known a priori (line connected

3

segments) and combines morphological operators to achieve the segmentation [17, 18, 19]. Although most of the state-of-the-art methods look for detecting all vessel pixels of the vascular tree, there are also some attempts based on finding the vessel skeleton, e.g., those based on shortest path connection [20], on matched filters [21], on ridge descriptors [22] or on the application of the classical marker-controlled watershed [23, 24], which differs to the stochastic watershed that is applied in this work.

The main contribution of this paper is the presentation of a complete methodology for significant point detection of the retinal vascular tree from a fundus image. It includes the vessel centerline extraction and the differentiation between bifurcations and complex crossings, which is a challenging and key process for a correct vessel tracking. In addition, despite the lack of public databases with manual-detected points to be used as ground truth, quantitative quality parameters were calculated.

The rest of the paper is organized as follows: Section 2 describes materials and methods. Section 3 presents an approach for vessel centerline extraction in retinal images. Section 4 addresses the algorithm to detect significant points on the vessel centerline. That algorithm is used to select the bifurcation points existing in the image and measure the bifurcation angles as explained in Section 5. Section 6 shows the results of the methods presented in Sections 3, 4 and 5. Finally, Section 7 closes the paper with conclusions and future lines of work.

2. Materials and Methods

2.1. Material

In this work, three different public databases were used: DRIVE [25], STARE [11] and VARIA [26]. DRIVE and STARE databases were used in the validation of the method for vessel centerline detection and all of them in the validation of significant point identification.

DRIVE database is composed of 40 retinal images (565 x 584 pixels) belonging to diabetic subjects. For each image, a mask image that delineates the field

of view is provided as well as manual segmentations of the blood vessels. STARE database is a set of 20 images (700 x 605 pixels) along with two hand-labelled vessel network provided by different experts. VARIA contains 233 images, from 139 different individuals, with a resolution of 768 x 584 pixels.

2.2. Morphological operators

Mathematical morphology is a non-linear image processing methodology based on minimum and maximum operations, which can be used to extract relevant structures of an image f [27]. This is achieved by probing the image with another known shape B called structuring element (SE). The result of the single operation also depends on the choice of B. The two basic morphological operators are: *dilation*, $\delta_B(f)$, and *erosion*, $\varepsilon_B(f)$. Their purpose is to expand light or dark regions, respectively, according to the size and shape of the SE. Those elementary operations can be combined to obtain a set of basic filters: *opening*, $\gamma_B(f)$, and closing, $\varphi_B(f)$. Light or dark structures are respectively filtered out from the image by these operators regarding the SE chosen.

The method proposed in this paper for vessel centerline detection applies these basic filters directly, or uses them to derive more complex operators, such as:

- *Dual top-hat transformation*, $\rho_B(f) = \varphi_B(f) - f$, is used to extract contrasted dark components with respect to the background.

- *Close-hole operator* fills all holes in an image f that do not touch a boundary image. For a grey-scale image, it is considered a hole any set of connected points surrounded by connected components of value strictly greater than the hole values. This operator is defined as $\psi^{ch}(f) = [\gamma^{rec}(f^c, f_\partial)]^c$, where $\gamma^{rec}(g, f)$ is the *reconstruction by dilation* of an image f (marker) which is contained within an image g (reference), f^c is the complement image (i.e., the negative) and f_∂ the image boundary.

- *Reconstruction by dilation*, $\gamma^{rec}(g, f) = \delta_g^{(i)}(f)$, is the successive geodesic dilation of f regarding g up to idempotence, so that $\delta_g^{(i)}(f)$ represents the

5

geodesic dilation and $\delta_g^{(i)}(f) = \delta_g^{(i+1)}(f)$. The *geodesic dilation*, $\delta_g^{(i)}(f) = \delta_g^{(1)}\delta_g^{(i-1)}(f)$, is the iterative unitary dilation of f regarding g, being $\delta_g^{(1)}(f) = \delta_B(f) \wedge g$.

2.3. Stochastic watershed transformation

Watershed transformation is a segmentation technique for gray-scale images [28]. This algorithm is a powerful segmentation tool whenever the minima of the image represent the objects of interest and the maxima are the separation boundaries between objects. Due to this fact, the input image of this method is usually a gradient image $\varrho(f)$. However, one problem of this technique is the over-segmentation, which is caused by the existence of numerous local minima in the image normally due to the presence of noise. One solution to this problem is using marker-controlled watershed, $WS(\varrho)_{f_{mrk}}$, in which the markers f_{mrk} artificially impose the minima of the input image. Nevertheless the controversial issue consists in determining f_{mrk} for each region of interest. Note that the use of a limited number of markers along with the complex morphology of the retinal vascular network can also cause that some parts of it are not detected (sub-segmentation). Therefore, the choice of the correct markers is crucial for the effectiveness and robustness of the algorithm.

The stochastic watershed is used to solve the sub-segmentation conflict [29]. In this transformation, a given number M of marker-controlled-watershed realizations are performed selecting N random markers to estimate a probability density function (*pdf*) of image contours and filter out non significant fluctuations. The results of the different realizations are averaged by Parzen window method [30]. Obtaining a *pdf* of the contours of the watershed regions facilitates the final segmentation, providing robustness and reliability since the arbitrariness in choosing the markers is avoided. Afterwards, it is necessary to perform a last marker-controlled watershed on the *pdf* obtained to obtain a final result. This type of watershed works better than other marker-based watershed transformations used previously in the literature.

2.4. Hit-or-miss transformation

Hit-or-miss transformation (HMT) is a morphological operator used for detecting specific patterns in a binary image [31]. Therefore, it can be applied to detect the significant points on a skeleton image. This is achieved by probing the image with a specific set of known shape (structuring element or SE). The structuring element employed in this operation is called composite structuring element since it contains two basic SE. The first one, denoted by B_{FG}, defines the set of pixels that should match the foreground (positive pixel values) while the second one, denoted by B_{BG}, defines the set of pixels that should match the background (zero pixel values). By definition, B_{FG} and B_{BG} share the same origin and are disjoint sets, i.e., $B_{FG} \cap B_{BG} = 0$. Depending on whether the origin belongs to B_{FG} or B_{BG} the HMT extracts foreground or background pixels [27]. Figure 1 depicts a composite structuring element $\mathbf{B} = (B_{FG}, B_{BG})$ where B_{FG} is denoted by 1's, B_{BG} by 0's and the rest of values are ignored. In this example, the HMT would detect the pixels with a neighbor on the left but that up, down and to the right did not have any. The value of the left diagonals does not matter, it could be 0 or 1.

	0	0
1	1	0
	0	0

B

=

0	0	0
1	1	0
0	0	0

B_{FG}

+

0	1	1
0	0	1
0	1	1

B_{BG}

Figure 1: Example of a composite structuring element.

The HMT of a set X by a composite structuring element $\mathbf{B} = (B_{FG}, B_{BG})$ can be written in terms of an intersection of two morphological erosions [27]:

$$HTM_B(X) = \varepsilon_{B_{FG}}(X) \cap \varepsilon_{B_{BG}}(X^c), \tag{1}$$

where X^c is the complement set of X (i.e., the negative).

7

3. Skeleton extraction

In general, the detection of retinal vascular network is necessary before analyzing vessel features. The most common approach in the literature is a first stage of vessel segmentation, then the skeletonization of the detected vessels and finally the analysis of different features on the vascular skeleton such as vessel calibers, significant points or bifurcation angles. The major drawback of this approach is the dependence of the different stages on the previous ones in addition to an increase of computational cost. Based on these facts, this section is focused on obtaining the retinal skeleton in a direct way avoiding the segmentation stage. Its goal is to reduce the number of necessary steps in the processing of the fundus image. As a consequence, this would also reduce the dependency of previous stages. Specifically, the method proposed for this purpose is mainly based on mathematical morphology along with curvature evaluation. Two main steps are involved: in the first step, the principal curvature is calculated on the retinal image. In the second step, the stochastic watershed transformation is applied to extract the vascular skeleton. The main stages are included in the flowchart shown in Figure 2.
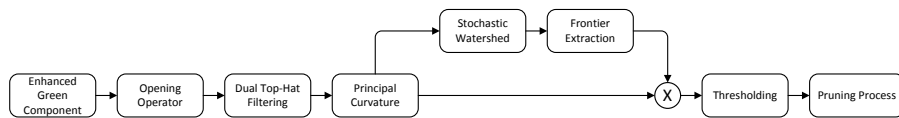

Figure 2: Flowchart for skeleton extraction.

Although fundus images are RGB format, the present work is drawn on monochrome images obtained from the green component extraction because this band provides improved visibility of the blood vessels. Moreover, this image is enhanced such that 1% of data is saturated at low and high intensities (Figure 3(a)). Then, a small opening, using a disc of radius 1 as SE (B_1), is performed on the enhanced green component image to fill in any gaps in vessels that could provoke subsequent errors, for example due to brighter zones within

arteries. Next, a dual top-hat, with a SE larger than the widest vessel (B_2), is applied with the goal of extracting all of them and eliminating structures with high gradient that are not vessels, as occurs in the optic disc (Figure 3(b)). Afterwards, with the aim of highlighting the vessels on the background, principal curvature is calculated as the maximum eigenvalue of the Hessian matrix H [9]:

$$H = \begin{pmatrix} \partial_{xx}f & \partial_{xy}f \\ \partial_{yx}f & \partial_{yy}f \end{pmatrix},$$ (2)

where $\partial_{ij}f$ represents the second directional derivatives of an image $f(x, y)$. The Hessian matrix is calculated at different scales ($s = \{0, 2, 8, 14\}$) by convolving the original image $f(x, y)$ with a Gaussian kernel G of variance s^2,

$$f_s(x, y; s) = f(x, y) * G(x, y; s) = f(x, y) * \frac{1}{2\pi s^2} e^{-\frac{x^2 + y^2}{2s^2}}.$$ (3)

The resulting image is shown in Figure 3(c).

If the principal curvature is directly calculated on the enhanced image, all structures with high curvature are highlighted, not only the vessels. The optic disk border has also high curvature but it should not be detected. This is a typical problem that occurs in most edge detection methods for vessel segmentation that it is avoided with the previous dual top-hat filtering.

Then, the principal curvature f_κ is obtained by normalizing each λ_{max} by $2s$ and computing the local maxima over scales:

$$f_\kappa = \max_s \left(\frac{\lambda_{max}(s)}{2s} \right).$$ (4)

Finally, stochastic watershed is applied to the curvature image. As explained above, this transformation uses random markers to build a probability density function (pdf) of contours (Figure 3(d)). In particular, 10 marker-controlled-watershed realizations were performed selecting 300 random markers in each realization. Then, pdf is segmented by a last marker-controlled watershed. The vascular skeleton is part of the frontiers of the resultant regions as can be observed in Figure 3(e).
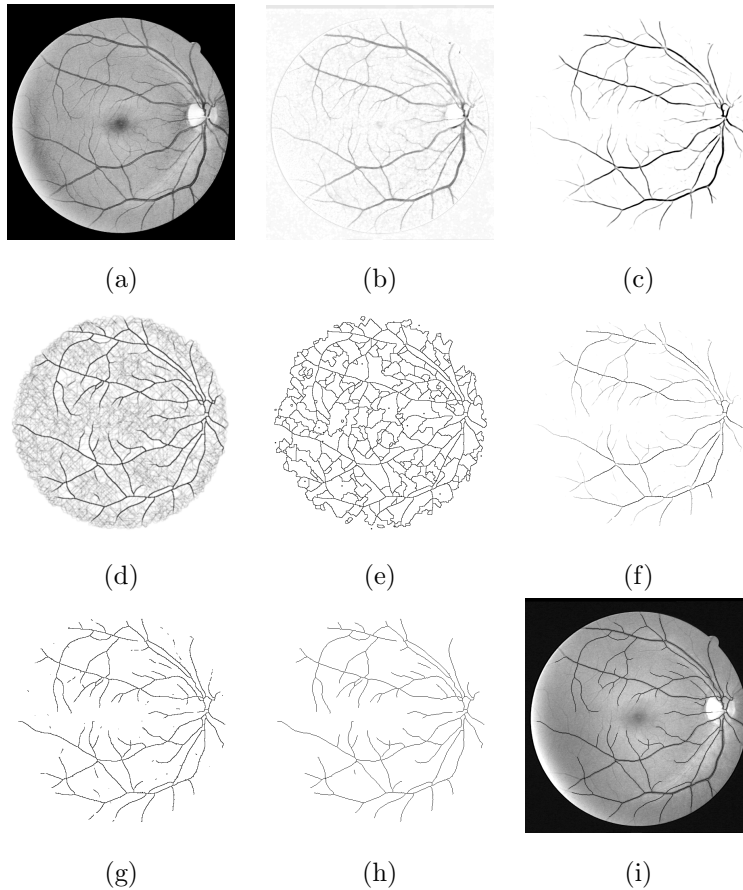
9

Figure 3: Skeleton extraction process: (a) Enhanced green component obtained from the original fundus image, (b) Dual top-hat filtering, (c) Principal curvature, (d) Probability density function (pdf) of contours obtained with 10 simulations and 300 random markers, (e) Watershed frontiers, (f) Product between the principal curvature and the watershed frontiers, (g) Thresholding ($t = 0.05$), (h) Pruning and (i) Final result. The images (b)-(h) have been inverted for better visualization.

In that case, both for *pdf* computing and for last marker-controlled watershed, random markers are combined with some controlled markers. This is due to the morphology of the vascular network which contains many of vessel crossings. In addition to the random markers, it is forced that there is one marker at least in the area delimited by the crossing of two vessels (controlled markers),

10

so that the final markers are directly the union of both (random and controlled markers). This methodology avoids that the vessels close to some crossing are not detected by the watershed transformation. The crossing areas are determined by means of the residue of the close-hole operator on f_κ and then one or more markers are chosen randomly within these areas giving place to the controlled markers. This problem is illustrated in Figure 4, where only a region of interest is shown for better visualization.
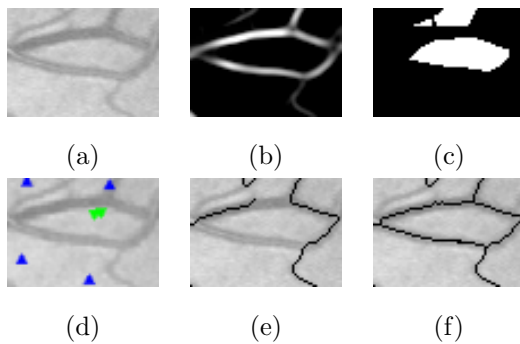

Figure 4: Stochastic watershed on the crossing of two vessels: (a) Enhanced green component, (b) Principal curvature (f_κ), (c) Residue of close-hole operator, (d) Random (blue ▲) and two controlled (green ▼) markers, (e) Result of the stochastic watershed using only the random markers shown in blue and (f) Result of the stochastic watershed combining random and controlled markers (blue and green).

In order to discriminate which frontiers are significant and which ones are not and should be filtered out, the frontiers are multiplied by f_κ (Figure 3(f)) and then are thresholded (Figure 3(g)) using a fixed threshold, experimentally $t = 0.05$. Once the skeleton is obtained, a pruning process is applied to remove possible spurs giving rise to the final result of the presented method (Figure 3(h) and 3(i)).

The implemented pruning process is characterized by removing spur branches but without altering the main branches. Only the branches whose size is less than a threshold ($n_{max} = 10$) are removed while the other are kept intact [32]. n_{max} value must be fixed based on image resolution. The pruning method is

based on defining a function $\Upsilon(S)$ which assigns to each point of the skeleton S the number n of unitary erosions needed to remove it from S. The value of the function $\Upsilon(S)$ is $n_{max} + 1$ for the points $\mathbf{x} \in S$ which are not removed after n_{max} unitary erosions. Then, making use of the function $\Upsilon(S)$, it is possible to differentiate between the secondary and the main skeleton branches. A branch is considered as secondary if $\Upsilon(S(\mathbf{x}_1)) - \Upsilon(S(\mathbf{x}_2)) > 1$, being $\mathbf{x}_1$ and $\mathbf{x}_2$ two adjacent points of the skeleton branch. Afterwards, the secondary branches are disconnected from the main branches and a reconstruction by dilation is applied using this image, i.e. the skeleton with the secondary branches disconnected, as reference and being the marker image that defined by Equation 5.

$$mrk = \begin{cases} 1 & \text{if } \Upsilon(S(\mathbf{x}))) = n_{max} + 1 \\ 0 & \text{otherwise} \end{cases} \tag{5}$$

This operation manages to reconstruct the original skeleton but without spur branches. Figure 5 shows an example of the main pruning steps and the difference between the proposed pruning and the conventional.

Algorithm 1 summarizes the steps of the vessel centerline extraction method and Algorithm 2 the steps of the pruning process.

4. Significant point determination

As mentioned before, in the vascular skeleton there are three types of significant points: terminal, bifurcation and crossing points. All of them must be detected due to their interest to characterize the relations between the different branches of the skeleton, i.e., relations between the parent and daughter branches.

4.1. Terminal and bifurcation points

The hit-or-miss transformation (HMT) can be directly applied to the vascular skeleton to locate terminal and bifurcation points using the different SE shown in Figure 6 and Figure 7. It must be remembered that B_{FG} is denoted by 1's and B_{BG} by 0's. Note that these SE must be used in all their orientations,
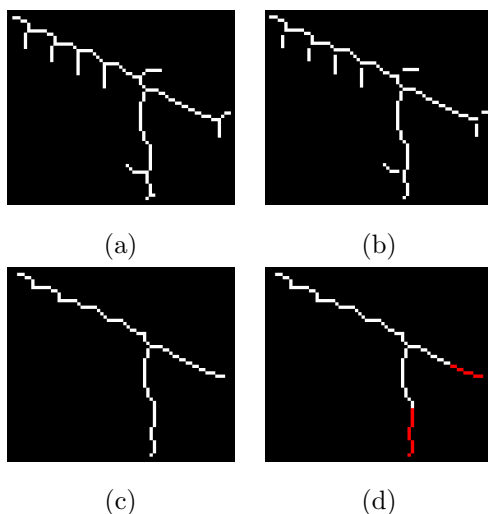
12

Figure 5: Pruning process: (a) Original skeleton, (b) Skeleton with the secondary branches disconnected, (c) Pruned skeleton by the proposed method and (d) Result of the conventional pruning (marked in red the pixels that are removed by the conventional pruning and are remained by the proposed pruning process). It can be observed that the main advantage of the proposed pruning is that only the spur branches are removed while the rest are kept intact. The conventional pruning removes a specific number of pixels for every branch (without taking into account its relevance).

one each $90°$, so four hit-or-miss iterations are required for each SE, i.e., a total of 8 and 16 SEs are used to detect terminal and bifurcation points, respectively.

Figure 6: Structuring elements used for detecting terminal points.

The choice of the SE shape is related to the topology of the point in question. For example, on the one hand, any terminal point will have only one neighbor and it will be rounded by background pixels and, on the other hand, a bifurcation point will have three neighbors located in particular positions. This can be appreciated clearly if the SE defined in Figure 7 are observed.

Algorithm 1: Vessel centerline extraction

Data: Original RGB fundus image $\mathbf{f} = (f_R, f_G, f_B)$, Scale vector

$\quad\quad \mathbf{s} = [0, 2, 8, 14]$, Gaussian kernel G

Result: Vessel centerline, f_{out}

initialization: $\mathbf{B_1}, \mathbf{B_2}$ (as main text) ;

$f_{in} \leftarrow f_G$ Green component selection ;

$f_{enh} \leftarrow \Gamma(f_{in})$ Image Enhancement ;

$f_{op} \leftarrow \gamma_{B_1}(f_{enh})$ Opening ;

$f_{dth} \leftarrow \rho_{B_2}(f_{op})$ Dual top-hat ;

Principal curvature:

for $i \leftarrow 1$ **to** $length(\mathbf{s})$ **do**

$\quad\quad f_{s_i} \leftarrow f_{dth} \otimes G(s_i)$;

$\quad\quad H_{s_i} \leftarrow H(f_{s_i})$;

$\quad\quad \lambda_{max_{s_i}} \leftarrow \max\{eig(H_{s_i})\}$;

$\quad\quad \lambda'_{max_{s_i}} \leftarrow \dfrac{\lambda_{max_{s_i}}}{2s_i}$;

end

$f_\kappa \leftarrow \max_{\mathbf{s}}\left(\lambda'_{max_{\mathbf{s}}}\right)$;

$f_{ws} \leftarrow WS(f_\kappa)_{f_{mrk}}$ Stochastic Watershed with random and controlled

markers ;

$f_{th} \leftarrow (f_\kappa \times f_{ws}) < t$ Thresholding ;

$f_{out} \leftarrow \Upsilon(f_{th})$ Pruning ;

Retinal skeleton is an one-pixel-thick structure fully 8-connected. However, when the significant points belonging to the skeleton are being looked for, it is wanted to avoid the multiple paths that are inherent in this type of connectivity. Therefore, before point detection, it is necessary to convert the skeleton from 8-connectivity to m-connectivity so that the multiple paths are removed [31].

A pixel p has four horizontal and vertical neighbors $N_4(p)$ and four diagonal neighbors $N_D(p)$. All these neighbors are called the 8-neighbors of p, denoted

---

Algorithm 2: Pruning process

Data: Image of the retinal skeleton with spur branches S

Result: Pruned skeleton S'

initialization: $n_{max} = 10$ (Size of the branches to be removed), B
(Unitary structuring element), N_8 (8-neighborhood) ;

for $\mathbf{x} \leftarrow 1$ **to** $length(S)$ **do**

    if $(\mathbf{x} \in \varepsilon_B^{(n-1)}(S(\mathbf{x})) \; \& \; (\mathbf{x} \notin \varepsilon_B^{(n)}(S(\mathbf{x})))$ *with* $n \leq n_{max}$ **then**

        $\Upsilon(\mathbf{x}) = n$;

    else if $(\mathbf{x} \in \varepsilon_B^{(n_{max})}(S(\mathbf{x})))$ **then** $\Upsilon(\mathbf{x}) = n_{max} + 1$;

    else if $(\mathbf{x} \notin (S(\mathbf{x})))$ **then** $\Upsilon(\mathbf{x}) = 0$;

end

$R = S$ Reference image ;

for $\mathbf{x} \leftarrow 1$ **to** $length(S)$ **do**

    if $\Upsilon(\mathbf{x}) - \Upsilon(N_8(\mathbf{x})_{N_8 \ni S}) > 1$ **then** $R(\mathbf{x}) = 0$ Disconnection of
    secondary branches ;

    if $\Upsilon(\mathbf{x}) == (n_{max} + 1)$ **then** $mrk(\mathbf{x}) = 1$ Marker image ;

    else $mrk(\mathbf{x}) = 0$;

end

$S' = \gamma^{rec}(R, mrk)$ Reconstruction by dilation ;

---

by $N_8(p)$. Two binary pixels p and q are 8-connected if q is in the set $N_8(p)$ but they are m-connected if

1. q is in $N_4(p)$, or

2. q is in $N_D(p)$ and $N_4(p) \cap N_4(q) = 0$.

The difference between 8-connectivity and m-connectivity can be appreciated in Figure 8. This conversion is necessary because the central pixel involves that there is not only a possible path in the skeleton therefore the detection of significant points and any tracking process performed later could be erroneous.

In the case of the 8-connectivity, the multiple paths are manifested in four
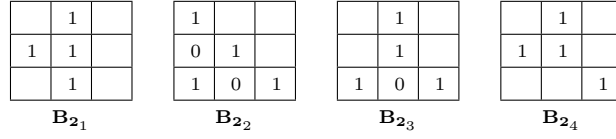
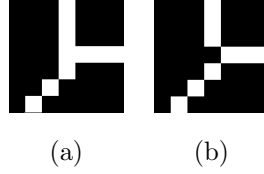Figure 7: Structuring elements used for detecting bifurcation points.

(a)   (b)

Figure 8: 8-connectivity to m-connectivity conversion (a) 8-connected skeleton and (b) m-connected skeleton.

basic patterns which are shown in Figure 9. It can be observed that the case shown in Figure 8 corresponds to the patterns $\mathbf{B_{3_2}}$ and $\mathbf{B_{3_3}}$.
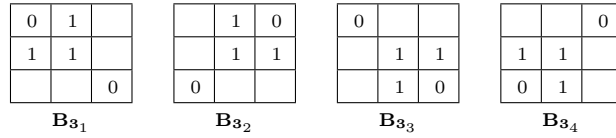

Figure 9: Structuring elements used to convert an 8-connected skeleton to m-connectivity.

The HMT allows to detect all these patterns. Then, the central pixels must be changed to 0 for eliminating the multiple paths. The conversion from 8 to m-connectivity can be performed through a basic sequence of morphological steps:

$$
\begin{aligned}
\Theta_1(X, \mathbf{B_{3_1}}) &= X - HMT_{\mathbf{B_{3_1}}}(X) = X \cap \left[HMT_{\mathbf{B_{3_1}}}(X) \right]^c \\
\Theta_2(\Theta_1, \mathbf{B_{3_2}}) &= \Theta_1 - HMT_{\mathbf{B_{3_2}}}(Y_1) = Y_1 \cap \left[HMT_{\mathbf{B_{3_2}}}(Y_1) \right]^c \\
\Theta_3(\Theta_2, \mathbf{B_{3_3}}) &= \Theta_2 - HMT_{\mathbf{B_{3_3}}}(Y_2) = Y_2 \cap \left[HMT_{\mathbf{B_{3_3}}}(Y_2) \right]^c \\
\Theta_4(\Theta_3, \mathbf{B_{3_4}}) &= \Theta_3 - HMT_{\mathbf{B_{3_4}}}(Y_3) = Y_3 \cap \left[HMT_{\mathbf{B_{3_4}}}(Y_3) \right]^c \\
\Theta(X, \mathbf{B_3}) &= \Theta_4,
\end{aligned}
\tag{6}
$$

where X is the input image that contains the 8-connected skeleton and Θ the

output image with the corresponding skeleton with m-connectivity.

4.2. Crossing points

Due to the fact that the intersections between different branches of the vascular tree are formed, usually, by a set of pixels, most crossing points cannot be detected by pattern recognition on the skeleton, i.e., through the hit-or-miss transformation. It can only be applied in simple crossing point detection using the SE shown in Figure 10.

0	1	0
1	1	1
0	1	0

$\mathbf{B_{4_1}}$

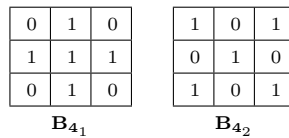| 1	0	1
0	1	0
1	0	1

$\mathbf{B_{4_2}}$

Figure 10: Structuring elements used for detecting simple crossing points.

However, practically most crossing points, if not all, are not simple, or in other words, the branches do not intersect in only one pixel and several points can belong to the same intersection. This provokes that the extremes of the intersection are considered as bifurcation because both of them have three neighbors and accomplishes some of the characteristic patterns of the bifurcation points. Figure 11 represents the different types of crossing points. The light gray branch intersects with other two branches, drawn in dark gray, giving rise to a simple (X) and a complex (O) crossing point marked in black.

Most works of the state-of-the-art consider that the vessel crossing points are two bifurcation points very close to each other. So, a fixed-size circular window is centered on the candidate bifurcations and if there exist four intersections between the window and the skeleton, the point is marked as a crossing. The problem of this approach is that the crossing point detection depends on a large degree on the window size. If the size is too small, the crossings are not detected and if the size is too big other vessels not belonging to this crossing can intersect with the window. Moreover, it must be taken into account that the size of the intersections varies from one case to another and it is also dependent on the image resolution.
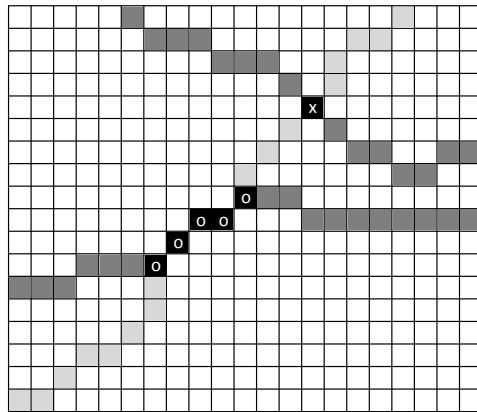
17

Figure 11: Different types of crossing points: simple (X) and complex (O).

Retinal vessels have their origin in the optic disk head. From this center, the vessels bifurcate and constitute the retinal vascular tree. It is common that arteries and veins intersect in some occasion and generate the crossing points under consideration (Figure 12(a)). This means that when they intersect, as the vessels have a common origin, generate a sort of close loop which will be useful to differentiate if one point is a crossing point or not (Figure 12(b)). Based on this idea, a new algorithm is proposed to analyze all points detected initially as a bifurcation in order to discriminate those that are really crossing points.
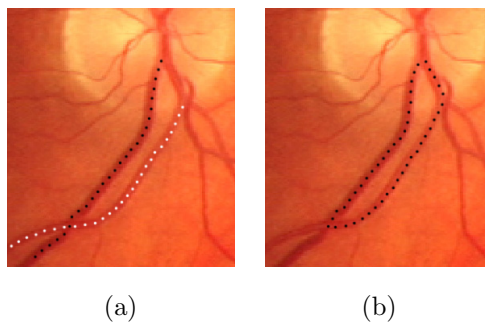

(a)   (b)

Figure 12: Vessel intersection: (a) Intersection between two vessels and (b) Close loop formed by an intersection.

First, a bifurcation point is considered as candidate to be a crossing point if when a circular window is centered on this point, there are four or more intersections between the skeleton and this window (W). The window radius is three times the average diameter of the vessels. This size is established empirically. Then, if the candidate point is part of a close loop generated by the skeleton branches, the closest candidate to crossing point is looked for, and if it is directly connected with the previous point and is not part of the same loop, both of them are established as crossing points. Figure 13 represents this process. Terminal and bifurcation points detected by the HMT are marked in red and green, respectively (Figure 13(a)). In Figure 13(b) the candidates to crossing points are highlighted in yellow. The close loops that contain some candidate point are drawn in Figure 13(c). Figure 13(d) shows the final result with the crossing points detected in white. Note that the two points identified in green at the bottom left of the Figure 13(d) are not crossing points but bifurcations because they do not accomplish the condition of belonging to a different loop. Both of them belong to the close loop marked in orange in Figure 13(c). To be considered as crossing, two candidates should be connected and belong to a different loop.

With this type of analysis, the more common intersection extremes are completely identified. In addition, it should be taken into account that the pixels between these points are also part of the same intersection.

Algorithm 3 summarizes the complete process of the detection of the significant points on the retinal vascular skeleton. $\mathbf{B_1}, \mathbf{B_2}, \mathbf{B_3}, \mathbf{B_4}$ are the composite structuring elements defined in Figures 6, 7, 9 and 10.

5. Use of the significant points: Measurement of bifurcation angles

The significant points of the retinal vascular tree can be used as biometric features, landmarks for registration or keypoints in tracking processes and branching patterns. In particular, this section presents an algorithm that makes use of the significant points detected as detailed in Section 4 to measure the bi-
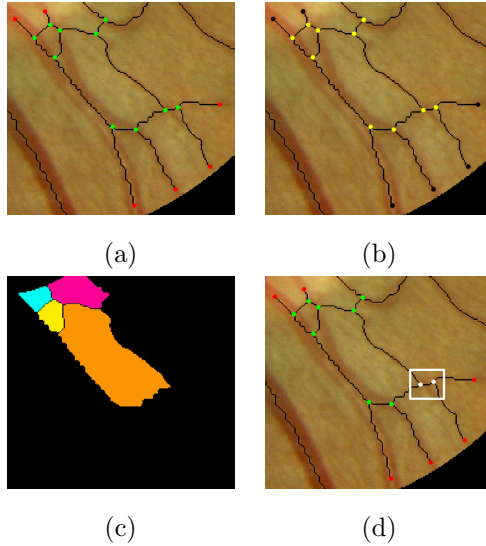
19

Figure 13: Automatic detection of common intersections: (a) Significant points detected by means of HMT (terminal points in red and bifurcation points in green), (b) Crossing point candidates, (c) Close loops formed by branches that contain some candidate point and (d) Crossing points automatically detected (white).

furcation angles.

The algorithm proposed to carry out this measurement is based on the estimation of the main orientations of the image gradient at each bifurcation point previously detected. The estimation of the multiple main orientations is performed as the flowchart depicted in Figure 14. This approach differs from [33], where the multiple main orientations are estimated by analysing a block of the image, whereas in this method the multiple orientations are estimated at each pixel.

Let $f(\mathbf{x}) : E \to \mathbb{R}$ be a gray-level image, where the support space is $E \subset \mathbb{Z}^2$ and the pixel coordinates are $\mathbf{x} = (x, y)$. Let us define $g(\mathbf{x})$ as the absolute value of the gradient of $f(\mathbf{x})$, i.e.,

$$g(\mathbf{x}) = \|\nabla f(\mathbf{x})\| = \sqrt{\left(\frac{\partial f(x,y)}{\partial x}\right)^2 + \left(\frac{\partial f(x,y)}{\partial y}\right)^2}. \tag{7}$$

The directional opening of $g(\mathbf{x})$ by a linear (symmetric) structuring element

Algorithm 3: Significant point detection

Data: Image of the retinal skeleton f, Circular window W

Result: Binary image of the terminal points f_{TP}, Binary image of the bifurcation points f_{BP}, Binary image of the crossing points f_{CP}

initialization: $\mathbf{B_1}, \mathbf{B_2}, \mathbf{B_3}, \mathbf{B_4}$ (as main text) ;

$f_m \leftarrow \Theta_{\mathbf{B_3}}(f)$ m-connectivity conversion ;

$f_{TP} \leftarrow HMT_{\mathbf{B_1}}(f_m)$ terminal point detection ;

$f_{BP} \leftarrow HMT_{\mathbf{B_2}}(f_m)$ bifurcation point detection ;

$f_{CP_1} \leftarrow HMT_{\mathbf{B_4}}(f_m)$ simple crossing point detection ;

complex crossing point detection:

for $i \leftarrow 1$ **to** $\sum(f_{BP})$ **do**

    if $\sum(W_{BP_i} * f_m) \geq 4$ **then**

        if $f_{BP_i} \in close\ loop$ **then**

            $f_{BP_j} \leftarrow argmin(dist(f_{BP_i}, f_{BP}))$;

            if $(f_{BP_i} is\ connected\ with\ f_{BP_j}) \& (loop(f_{BP_i}) \neq loop(f_{BP_j}))$

            then

                $f_{CP_{2_i}} = f_{BP_i} + f_{BP_j}$;

            end

        end

    end

end

$f_{CP} = f_{CP_1} + f_{CP_2}$ crossing point detection ;

(SE) of length l and direction θ is defined as the directional erosion of g by $L^{\theta,l}$ followed by the directional dilation with the same SE [34]:

$$\gamma_{L^{\theta,l}}(g)(\mathbf{x}) = \delta_{L^{\theta,l}} \left[\varepsilon_{L^{\theta,l}}(g) \right](\mathbf{x}), \tag{8}$$
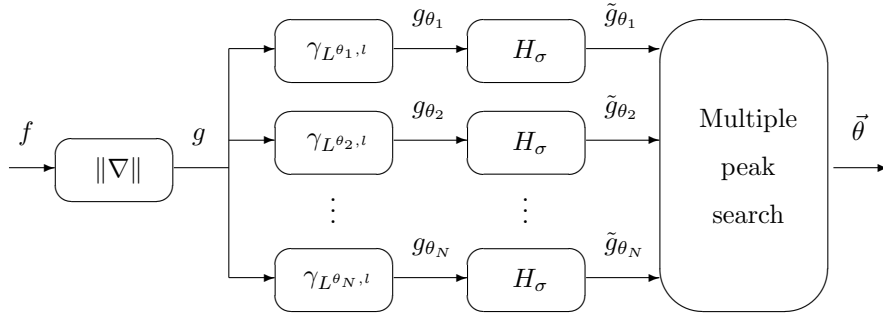
Figure 14: Flowchart of the multiple orientation estimation method.

where the directional erosion and dilation are respectively

$$\varepsilon_{L^{\theta,l}}(f)(\mathbf{x}) \quad = \quad \bigwedge_{\mathbf{h} \in L^{\theta,l}(\mathbf{x})} \{f(\mathbf{x}+\mathbf{h})\}, \tag{9}$$

$$\delta_{L^{\theta,l}}(f)(\mathbf{x}) \quad = \quad \bigvee_{\mathbf{h} \in L^{\theta,l}(\mathbf{x})} \{f(\mathbf{x}-\mathbf{h})\}. \tag{10}$$

The proposed orientation model is based on a decomposition of the gradient information by families of linear openings, $\{\gamma_{L^{\theta_i,l}}\}_{i \in I}$, according to a particular discretization of the orientation space $\{\theta_i\}_{i \in I}$.

In the next step of the proposed method, a filtering is performed at each one of the directional openings (depicted as H_σ in Figure 14). The filtering diffuses the orientation information and avoids angle mismatches due to noise. The kernel H_σ is the sampling of the gaussian low-pass filter

$$H_\sigma(\omega_1, \omega_2) = e^{-\frac{\sigma^2(\omega_1^2 + \omega_2^2)}{2}}, \tag{11}$$

where σ is the spatial standard deviation of the filter. More details of the method can be found in [35].

Once the directional openings have been filtered, the directional signature at pixel $\mathbf{x}$ is defined as

$$s_{\mathbf{x};l}(i) = \tilde{g}_{\theta_i}(\mathbf{x}). \tag{12}$$

Then, $s_{\mathbf{x};l}(i)$ is interpolated using cubic b-splines and its maxima correspond

to the multiple orientations existing at pixel $\mathbf{x}$. Finally, collecting all the orientations estimated at all the pixels in the image provides the multidimensional vector field $\vec{\theta}(\mathbf{x})$, see Figure 15.

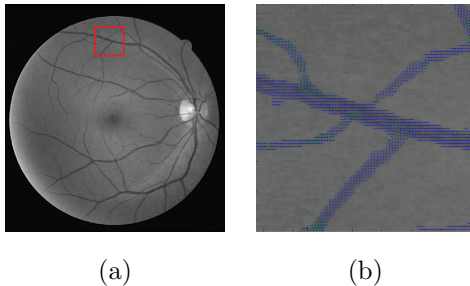
<div align="center">(a)   (b)</div>

Figure 15: Orientation vector field: (a) Green component of the original fundus image, (b) close-up of the image with its estimated multiple orientation vector field.

The bifurcation angles are calculated by performing the difference between the orientation vectors of each branch around the bifurcation points previously detected. An interior point is chosen as representative of each branch, and its orientation vector will define the orientation of the branch at this pixel. To obtain the interior points, a circular window is placed at each bifurcation and the intersection between the skeleton of the branch and the window is selected. Note that the choice of this pixel is not critical since the orientation vector field varies slowly inside the vessel. Due to the discretization of the orientation space of the multiple orientation method, the orientation is estimated using the ASGVF method [34] which achieves a higher angular resolution than the approach introduced in [33]. Since the ASGVF method only estimates the orientation and it is defined between $-90°$ and $90°$ degrees, the direction of each vector can be obtained taking into account the location of the representative pixel of each branch in relation to the centre of the bifurcation. Considering the quadrant of the representative pixel, the direction of the vector can be obtained, providing a vector field which is defined between $0°$ and $360°$ degrees. Finally, after the conversion of the orientation space, it is possible to calculate the angular difference between the branches contained in the window and thus

to obtain a measure of the bifurcation angle.

6. Results

6.1. Skeleton

The validation of the skeleton method was carried out on DRIVE [25] and STARE [11] databases. Although, in both databases, manual segmentations are included, these segmentations correspond to the complete vasculature not to the vessel centerline which is the goal of this work. For that reason, the homotopic skeleton [27] associated to the hand segmentations was obtained for future comparisons. In Figure 16, the results on some representative images from DRIVE and STARE databases can be observed.

(a)   (b)

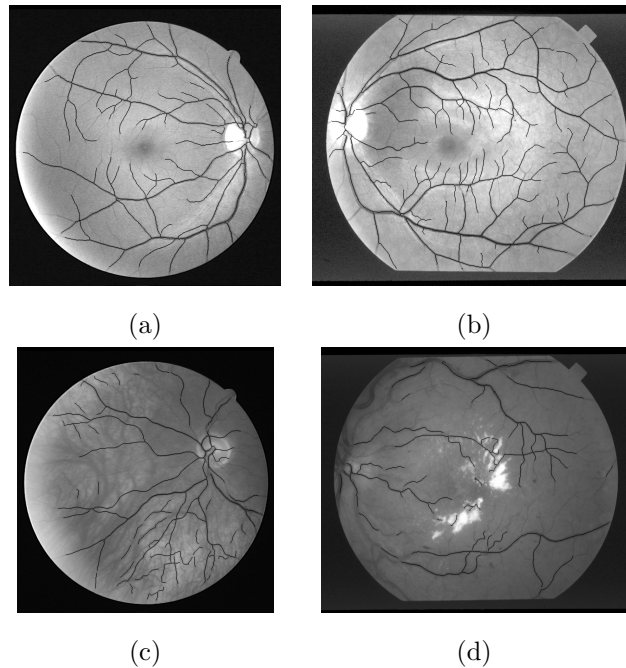(c)   (d)

Figure 16: Skeleton results of the proposed method: (a,c) DRIVE images ('19_test' and '23_training') and (b,d) STARE images ('im0255' and 'im0001').

The proposed method was compared with other state-of-the-art methods in two different ways. One approach is based on comparing the results of this work

with methods that firstly segment the vessels and then perform a skeletization process and the other comparison is performed with algorithms that obtain the skeleton directly.

On the one hand, regarding the methods that require a previous segmentation, the presented algorithm was compared with two methods previously published. The first compared method, proposed by Martinez *et al.* [9], uses the local maxima over scales of the magnitude of the gradient and the maximum principal curvature of the Hessian tensor in a multiple pass region growing procedure. The other method analysed in the comparison is the work of Morales *et al.* [7]. As the proposed method, it is based on mathematical morphology and curvature evaluation although the morphological operations used are different as well as the obtained result. In the same way as explained above, the homotopic skeleton was performed after the segmentation process in both cases. On the other hand, as for the methods that obtain directly the retinal vessel centerline, the analysis was focused on two approaches proposed by Walter and Klein method [23] and Bessaid *et al.* method [24] which are based also on the watershed transformation. In Figures 17 and 18, the results of the proposed method on two representative cases extracted from both databases are compared with the results of the state-of-the-art methods mentioned previously.

Avoiding complete vessel segmentation supposes an improvement in the automatic fundus processing since the skeleton is not dependent of a previous stage and the computational cost is reduced by decreasing the number of required steps. Apart from this fact, it must be stressed that an important advantage of the proposed method is its performance in pathological images or with large changes in illumination, as observed in Figure 17 and 18. In those cases, the algorithm presented in this paper works properly and reduces over-segmentation problems which can be found in methods based on a previous segmentation as [9, 7]. With regard to other methods that obtain the skeleton in a direct way and use the watershed transformation instead of the stochastic watershed [23, 24], the proposed work achieves a more robust detection and decreases the number of spurs. Despite good results, it must be mentioned that the main disadvantage
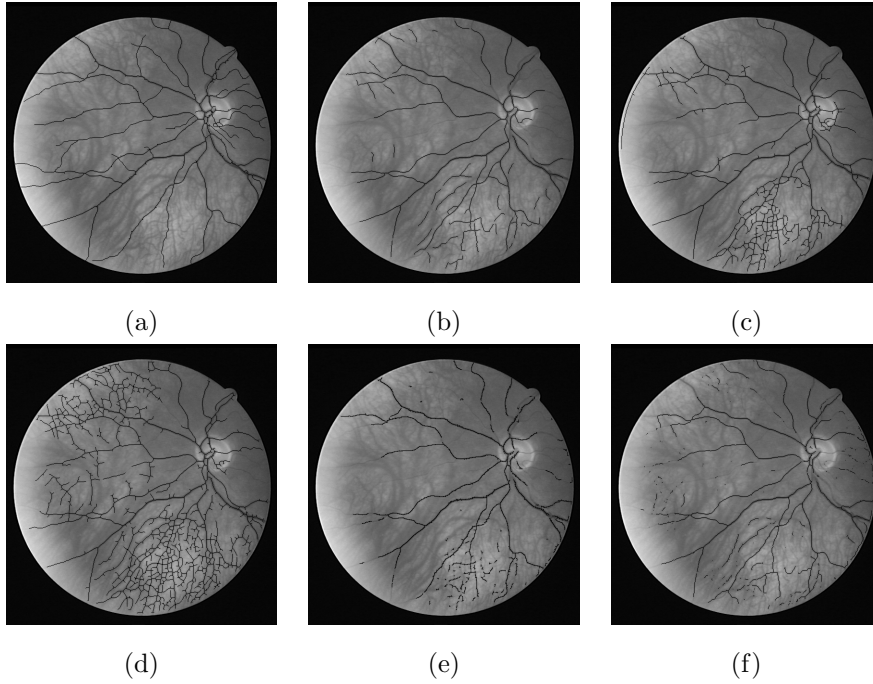
Figure 17: Comparison between different methods on DRIVE image ('23_training'): (a) Ground-truth skeleton, (b) Proposed method, (c) Martinez *et al.* method [9], (d) Morales *et al.* method [7], (e) Bessaid *et al.* method [24] and (f) Walter and Klein method [23].

of the method is that some vessels can lose their continuity if some part of them are not detected and it should be corrected in a post-processing stage.

6.2. Significant points

The validation of the method was carried out on a set of images randomly extracted from VARIA [26], DRIVE [25] and STARE [11] databases. Our results were compared with those provided by the method presented by Calvo *et al.* [8]. To the best of the author's knowledge, it was the state-of-the-art work that provides the best results in this issue and overcames the problems of other works of the literature. In Figure 19, the significant points detected on some representative images of the database can be observed.

The performance of both methods was evaluated based on four concepts: sen-
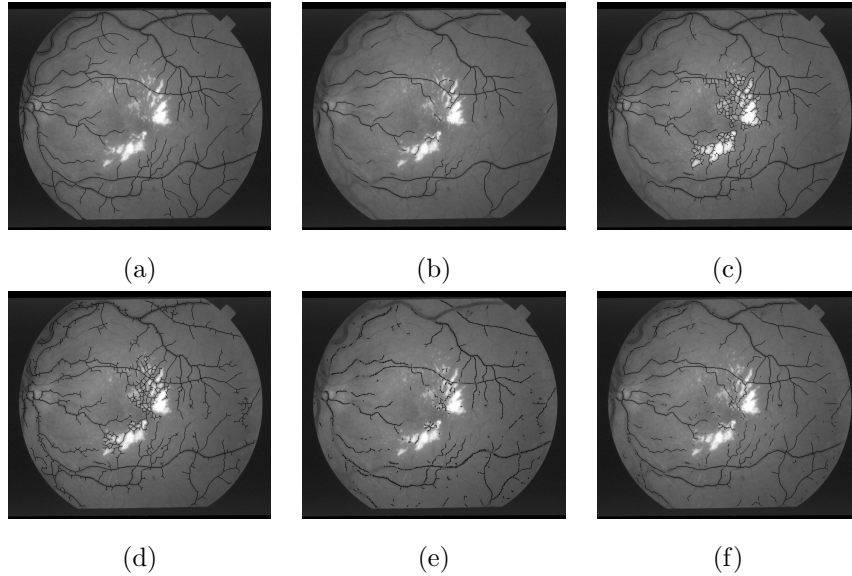
Figure 18: Comparison between different methods on STARE image ('im0001'): (a) Ground-truth skeleton, (b) Proposed method, (c) Martinez *et al.* method [9], (d) Morales *et al.* method [7], (e) Bessaid *et al.* method [24] and (f) Walter and Klein method [23].

sitivity or true positive rate (TPR), precision or positive predictive value (PPV), specificity or true negative rate (TNR) and negative predictive value (NPV). Sensitivity and specificity measure the proportion of positives/negatives that are correctly classified ($TPR = \frac{TP}{TP+FN}$; $TNR = \frac{TN}{TN+FP}$), PPV and NPV assess the quality of the positive/negative results ($PPV = \frac{TP}{TP+FP}$; $NPV = \frac{TN}{TN+FN}$). TP, FP, TN and FN are the true positives, false positives, true negatives and false negatives, respectively. Table 1 and Table 2 detail the values of these parameters for the bifurcation and crossing point detection of the images shown in Figure 19. Table 3 gathers the results of the same analysis but considering at the same time bifurcations and crossovers. Note that, in the validation, only one crossing point is counted for each intersection although if the crossing between two vessels is large enough, the start and end point of the intersection can be observed in the image. Table 4 summarizes the averaged results of the previous tables. From a general point of view, the results of the proposed

27

(a)   (b)   (c)   (d)

(e)   (f)   (g)   (h)

(i)   (j)   (k)   (l)
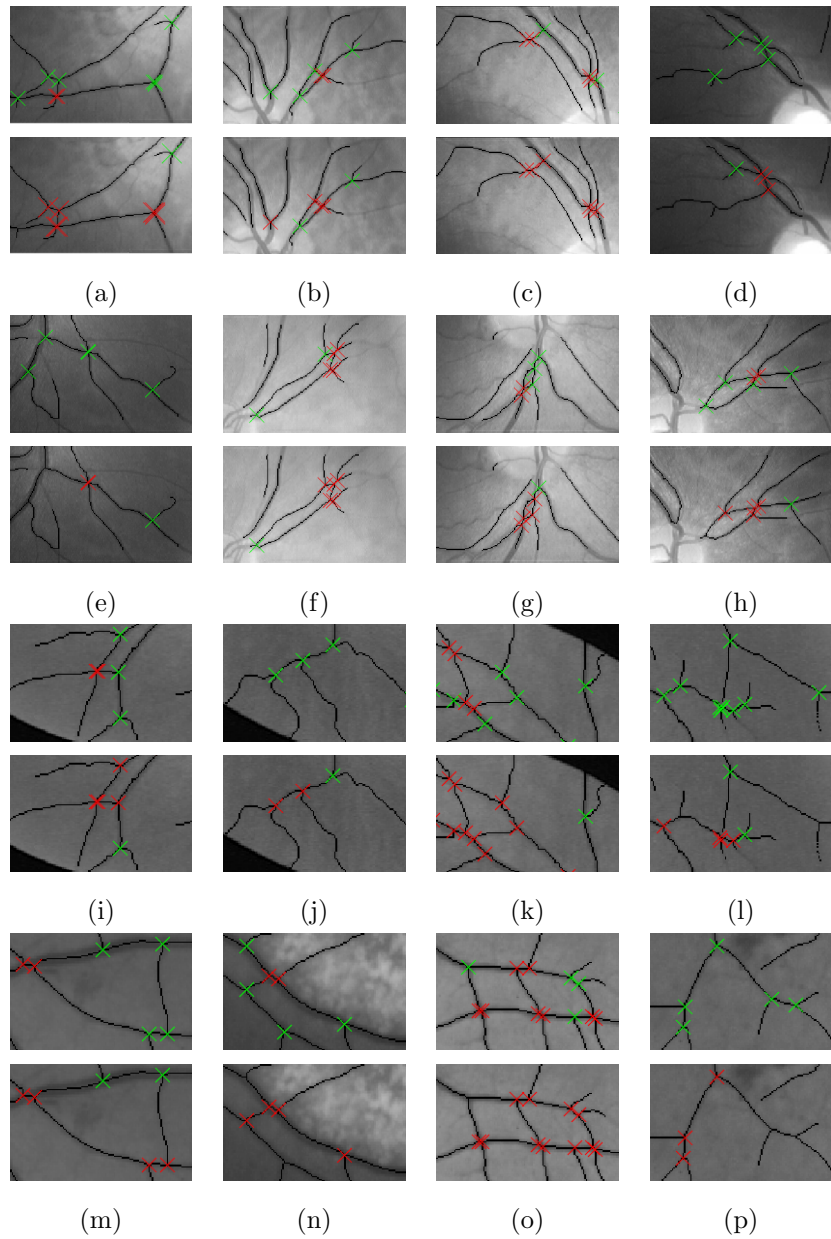
(m)   (n)   (o)   (p)

Figure 19: Bifurcation and crossing point detection on images belonging to VARIA, DRIVE and STARE databases: (a-h) Regions of interest of different images. Top row: results provided by the proposed method. Bottom row: results provided by the method presented in [8]. Bifurcation points are marked in green and crossovers in red.

method are better than the method of Calvo *et al.* achieving a $TPR = 1.000$ and a $PPV = 0.908$ for global point detection, i.e. considering bifurcations and crossovers. To point out that the proposed method provides balanced results in terms of TPR, PPV, TNR and NPV for bifurcation and crossing point detection. However, the method of Calvo *et al.* has high sensitivity (TPR) but low specificity (TNR) for crossing detection and vice versa for bifurcations. This is due to the fact that the method of Calvo *et al.* detects numerous false positives and negatives in crossing and bifurcation detection, respectively.

Table 1: Results for bifurcation point detection: true positives (TP), true negative (TN), false positives (FP), false negatives (FN), true positive rate (TPR), positive predictive value (PPV), true negative rate (TNR) and negative predictive value (NPV).

	Figure	TP	TN	FN	FP	TPR	PPV	TNR	NPV
Proposed method	19(a)	5	1	0	0	1.000	1.000	1.000	1.000
	19(b)	4	1	0	0	1.000	1.000	1.000	1.000
	19(c)	2	2	0	0	1.000	1.000	1.000	1.000
	19(d)	3	0	0	1	1.000	0.750	0.000	-
	19(e)	3	0	0	1	1.000	0.750	0.000	-
	19(f)	2	1	2	0	0.500	1.000	1.000	0.333
	19(g)	3	1	0	0	1.000	1.000	1.000	1.000
	19(h)	4	1	0	0	1.000	1.000	1.000	1.000
	19(i)	3	1	0	0	1.000	1.000	1.000	1.000
	19(j)	3	0	0	0	1.000	1.000	-	-
	19(k)	5	2	0	0	1.000	1.000	1.000	1.000
	19(l)	6	0	0	1	1.000	0.857	0.000	-
	19(m)	3	1	0	1	1.000	0.750	0.500	1.000
	19(n)	4	1	0	0	1.000	1.000	1.000	1.000
	19(o)	4	3	2	0	0.667	1.000	1.000	0.600
	19(p)	5	0	0	0	1.000	1.000	-	-
Calvo *et al.* [8]	19(a)	1	1	4	0	0.200	1.000	1.000	0.200
	19(b)	2	1	2	0	0.500	1.000	1.000	0.333
	19(c)	0	2	2	0	0.000	-	1.000	0.500
	19(d)	1	1	2	0	0.333	1.000	1.000	0.333
	19(e)	1	1	2	0	0.333	1.000	1.000	0.333
	19(f)	1	1	3	0	0.250	1.000	1.000	0.250
	19(g)	1	1	2	0	0.333	1.000	1.000	0.333
	19(h)	1	1	3	0	0.250	1.000	1.000	0.250
	19(i)	1	1	2	0	0.333	1.000	1.000	0.333
	19(j)	1	0	2	0	0.333	1.000	-	0.000
	19(k)	1	2	4	0	1.000	1.000	1.000	0.333
	19(l)	2	1	4	0	0.333	1.000	1.000	0.200
	19(m)	2	2	1	0	0.667	1.000	1.000	0.667
	19(n)	0	1	4	0	0.000	-	1.000	0.200
	19(o)	0	3	6	0	0.000	-	1.000	0.333
	19(p)	0	0	5	0	1.000	1.000	-	0.000

Table 2: Results for crossing point detection: true positives (TP), true negative (TN), false positives (FP), false negatives (FN), true positive rate (TPR), positive predictive value (PPV), true negative rate (TNR) and negative predictive value (NPV).

	Figure	TP	TN	FN	FP	TPR	PPV	TNR	NPV
Proposed method	19(a)	1	5	0	0	1.000	1.000	1.000	1.000
	19(b)	1	4	0	0	1.000	1.000	1.000	1.000
	19(c)	2	2	0	0	1.000	1.000	1.000	1.000
	19(d)	0	3	1	0	0.000	-	1.000	0.750
	19(e)	0	3	1	0	0.000	-	1.000	0.750
	19(f)	1	2	0	2	1.000	0.333	0.500	1.000
	19(g)	1	3	0	0	1.000	1.000	1.000	1.000
	19(h)	1	4	0	0	1.000	1.000	1.000	1.000
	19(i)	1	3	0	0	1.000	1.000	1.000	1.000
	19(j)	0	3	0	0	-	-	1.000	1.000
	19(k)	2	5	0	0	1.000	1.000	1.000	1.000
	19(l)	0	6	1	0	0.000	-	1.000	0.857
	19(m)	1	3	1	0	0.500	1.000	1.000	0.750
	19(n)	1	4	0	0	1.000	1.000	1.000	1.000
	19(o)	3	4	0	2	1.000	0.600	0.667	1.000
	19(p)	0	5	0	0	-	-	1.000	1.000
Calvo et al. [8]	19(a)	1	2	0	3	1.000	0.250	0.400	1.000
	19(b)	1	2	0	2	1.000	0.333	0.500	1.000
	19(c)	2	0	0	2	1.000	0.500	0.000	-
	19(d)	1	2	0	1	1.000	0.500	0.667	1.000
	19(e)	1	3	0	0	1.000	1.000	1.000	1.000
	19(f)	1	1	0	3	1.000	0.250	0.250	1.000
	19(g)	1	1	0	2	1.000	0.333	0.333	1.000
	19(h)	1	2	0	2	1.000	0.333	0.500	1.000
	19(i)	1	1	0	2	1.000	0.333	0.333	1.000
	19(j)	0	1	0	2	-	0.000	0.333	1.000
	19(k)	2	1	0	4	1.000	0.333	0.200	1.000
	19(l)	1	4	0	2	1.000	0.333	0.667	1.000
	19(m)	2	2	0	1	1.000	0.667	0.667	1.000
	19(n)	1	2	0	2	1.000	0.333	0.500	1.000
	19(o)	3	1	0	5	1.000	0.375	0.167	1.000
	19(p)	0	2	0	3	-	-	0.400	1.000

6.3. Bifurcation angles

The performance of the method proposed for bifurcation angle computation was evaluated on images belonging to DRIVE database [25]. In Figure 20, the angles measured on two representative images of this database can be observed. Only a region of interest of these images is shown for better visualization.

Table 3: Results for global significant point detection: true positives (TP), false positives (FP), false negatives (FN), true positive rate (TPR) and positive predictive value (PPV).

	Figure	TP	FN	FP	TPR	PPV
Proposed method	19(a)	6	0	0	1.000	1.000
	19(b)	5	0	0	1.000	1.000
	19(c)	4	0	0	1.000	1.000
	19(d)	3	0	1	1.000	0.750
	19(e)	3	0	1	1.000	0.750
	19(f)	3	0	2	1.000	0.600
	19(g)	4	0	0	1.000	1.000
	19(h)	5	0	0	1.000	1.000
	19(i)	4	0	0	1.000	1.000
	19(j)	3	0	0	1.000	1.000
	19(k)	7	0	0	1.000	1.000
	19(l)	6	0	1	1.000	0.857
	19(m)	4	0	1	1.000	0.800
	19(n)	5	0	0	1.000	1.000
	19(o)	7	0	2	1.000	0.778
	19(p)	5	0	0	1.000	1.000
Calvo et al. [8]	19(a)	2	1	3	0.667	0.400
	19(b)	3	0	2	1.000	0.600
	19(c)	2	0	2	1.000	0.500
	19(d)	2	1	1	0.667	0.667
	19(e)	2	2	0	0.500	1.000
	19(f)	2	0	3	1.000	0.400
	19(g)	2	0	2	1.000	0.500
	19(h)	2	1	2	0.667	0.500
	19(i)	2	0	2	1.000	0.500
	19(j)	1	0	2	1.000	0.333
	19(k)	3	0	4	1.000	0.429
	19(l)	3	2	2	0.600	0.600
	19(m)	4	0	1	1.000	0.800
	19(n)	1	2	2	0.333	0.333
	19(o)	3	1	5	0.750	0.375
	19(p)	0	2	3	0.000	0.000

Table 4: Averaged results for bifurcation, crossing and global point detection: true positive rate (TPR), positive predictive value (PPV), true negative rate (TNR) and negative predictive value (NPV).

	Bifurcations				Crossings				Global	
Method	TPR	PPV	TNR	NPV	TPR	PPV	TNR	NPV	TPR	PPV
Proposed	0.948	0.944	0.750	0.903	0.750	0.903	0.948	0.944	1.000	0.908
Calvo et al. [8]	0.367	1.000	1.000	0.288	1.000	0.392	0.432	1.000	0.761	0.496

The method was applied directly to the green component of the original RGB image. The directional openings were performed using an oriented linear structuring element of 7 pixels. This length comes from the trade-off between the curvature of the vessels and the angular resolution of the structuring element (it
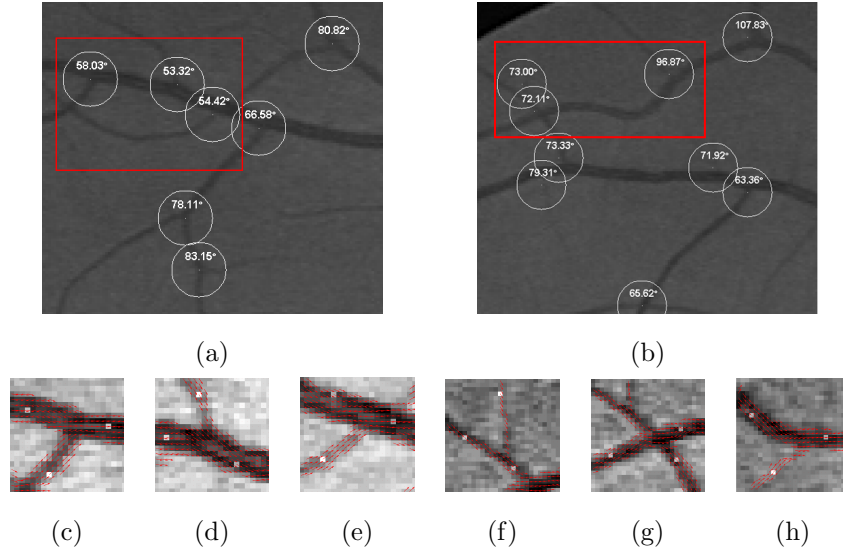
Figure 20: Angles of the bifurcations with the ASGVF orientation vector field on two images from DRIVE database. (a) A region of interest of the '*19 test*' image. (b) A region of interest of the '*40 training*' image. (c)-(e) Close up of selected bifurcations marked in red in (a). (f)-(h) Close up of selected bifurcations marked in red in (b). The bright pixels inside the vessels indicate at what points the value of the vector field were taken.

provides $\Delta\theta = 15°$ and produces a filter bank with 12 branches). The low-pass filtering of the directional openings is performed using σ=1. The parameters of the orientation estimation were chosen to deal with the particular resolution of DRIVE database (565×584). However, the orientation estimation method can be improved by considering a multiscale approach as described in [33]. There, the estimation of the orientation properties is provided by directional openings by line segments of variable length, which produce directional signatures for various scales.

In this paper, two methods for the computation of bifurcation angles were compared: the proposed method based on the orientation vector field and the method described in [7]. The main difference is that [7] requires to fit the branches of the skeleton by straight lines to measure the bifurcation angles. Moreover, it needs to perform a tracking process of the branches that compose

the retinal tree to distinguish between parent and daughter branches. Afterwards, the bifurcation angles are measured as the angles formed by the daughter branches of each bifurcation point. Specifically, the branches are fitted by straight lines using least-squares in a circular window centred on these points. The main drawback of this type of methods is its excessive dependence between the skeleton pixels and the measured angle. Figure 21 shows the measured angles provided by the method described in [7] on different expert hand-made segmentations.

Comparing the results shown in Figure 21, it can be appreciated that the measured angles can be quite different, reaching a maximum angle variation on the same image of around 7% in the Figure 21(a) and around 6% in the Figure 21(b). Note that the variation is due to the fact that the fitted line of the branches depends directly on the skeleton pixels considered. Only the change in one pixel of the skeleton can modify the fitted line and therefore the calculated angle. The angles shown in the Figure 21(a) and 21(b) correspond with the existing bifurcations within the red rectangles of the Figure 20(a) and 20(b) respectively. Since the method proposed in this paper is based on the main orientations and avoids the linear fitting of the branches, the provided measurements are much more accurate, stable and faithful to reality.

7. Conclusions

In this paper, a method for significant point detection of the retinal vascular tree was presented. Bifurcation and crossover identification is a difficult task due to the complexity of the vascular network. The most challenging part is the correct identification of the crossing points. This work proposes the use of hit-or-miss transformation (HTM) to detect terminal, bifurcation and simple crossing points. However, this transformation does not allow to characterize complex intersections, which are the most common in the vascular network. To deal with this problem, a post-processing stage is carried out on the points detected initially as bifurcations. The main idea to differentiate between a bifurcation
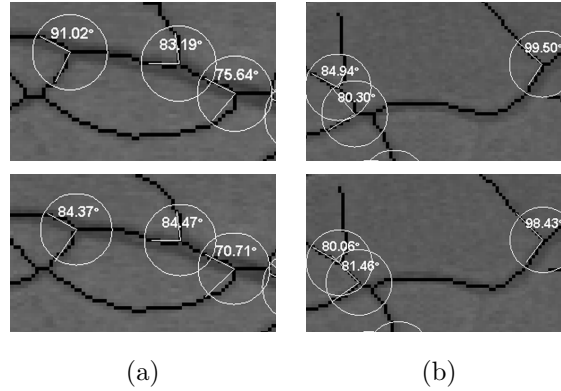
Figure 21: Bifurcation angles provided by the method described in [7] on the selected bifurcations of the Figure 20. This method is based on the skeletonization of a segmented (binary) image. (a) Skeletonization of two different expert segmentations of the '*19 test*' image. (b) Skeletonization of of two different expert segmentations of the '*40 training*' image. Slight differences in the skeleton cause large differences in the measured angles.

and a crossing point is that the crossing points belong to a sort of close loop formed by the intersection of two vessels.

The significant points of the retinal network must be detected on the vessel centerline. So, a method to determine the vascular skeleton on a fundus image was also proposed. It is based on mathematical morphology and curvature evaluation and makes use of the stochastic watershed to extract the vessel centerline in a direct way.

Then, the bifurcation points that were detected as the method presented in the paper were used later to measure the bifurcation angles of the retinal vascular tree through the multiple orientation vector field of each branch.

The performance of the method for significant retinal point detection was compared with other work of the literature. Quantitative quality parameters in point identification were calculated despite the difficulty in validation due to the lack of public databases that include ground-truth points. The obtained results demonstrate that our approach works properly for bifurcation and crossover detection. Note that the method of Calvo *et al.* detected numerous false negatives

34

and positives in the identification of the bifurcation and crossing points, respectively. If the performance of the global significant point detection is considered, our method detects more true positives and fewer false positives and negatives.

The algorithms presented for skeleton extraction and bifurcation angle measurement were also validated achieving promising results.

As future work, a wider validation of the significant point method should be performed. A ground truth of the significant points should be generated to carried out this validation. If the ground truth was publicly available, the comparison between methods would be facilitated.

Acknowledgments

References

[1] M. M. Fraz, P. Remagnino, A. Hoppe, B. Uyyanonvara, A. Rudnicka, C. Owen, S. Barman, Blood vessel segmentation methodologies in retinal images: A survey, Computer Methods and Programs in Biomedicine 108 (1) (2012) 407 – 433.

[2] J. Kanski, B. Bowling, Clinical Ophthalmology: A Systematic Approach, 7th Edition, Elsevier Health Sciences, 2011.

[3] A. Bhuiyan, B. Nath, J. Chua, K. Ramamohanarao, Automatic detection of vascular bifurcations and crossovers from color retinal fundus images, in: Signal-Image Technologies and Internet-Based System, 2007. SITIS '07. Third International IEEE Conference on, 2007, pp. 711–718.

[4] G. Azzopardi, N. Petkov, Detection of retinal vascular bifurcations by trainable v4-like filters, in: P. Real, D. Diaz-Pernil, H. Molina-Abril,

A. Berciano, W. Kropatsch (Eds.), Computer Analysis of Images and Patterns, Vol. 6854 of Lecture Notes in Computer Science, Springer Berlin Heidelberg, 2011, pp. 451–459.

[5] V. Bevilacqua, S. Cambò, L. Cariello, G. Mastronardi, A combined method to detect retinal fundus features, in: Proceedings of IEEE European Conference on Emergent Aspects in Clinical Data Analysis, 2005, pp. 1–6.

[6] M. E. Martinez-Perez, A. D. Hughes, A. V. Stanton, S. A. Thorn, N. Chapman, A. A. Bharath, K. H. Parker, Retinal vascular tree morphology: A semi-automatic quantification, in: Biomedical Engineering, Vol. 49, 2002.

[7] S. Morales, V. Naranjo, A. Navea, M. Alcañiz, Computer-aided diagnosis software for hypertensive risk determination through fundus image processing, Biomedical and Health Informatics, IEEE Journal of 18 (6) (2014) 1757–1763.

[8] D. Calvo, M. Ortega, M. G. Penedo, J. Rouco, Automatic detection and characterisation of retinal vessel tree bifurcations and crossovers in eye fundus images, Computer Methods and Programs in Biomedicine 103 (1) (2011) 28 – 38.

[9] M. E. Martinez-Perez, A. D. Hughes, S. A. Thom, A. A. Bharath, K. H. Parker, Segmentation of blood vessels from red-free and fluorescein retinal images, Medical Image Analysis 11 (2007) 47–61.

[10] X. Jiang, D. Mojon, Adaptive local thresholding by verification-based multithreshold probing with application to vessel detection in retinal images, IEEE Trans. Pattern Anal. Mach. Intell. 25 (2003) 131–137.

[11] A. Hoover, V. Kouznetsova, M. Goldbaum, Locating blood vessels in retinal images by piecewise threshold probing of a matched filter response, IEEE Transactions on Medical Imaging 19 (2000) 203–210.

[12] M. Al-Rawi, M. Qutaishat, M. Arrar, An improved matched filter for blood vessel detection of digital retinal images, Computers in Biology and Medicine 37 (2) (2007) 262–267.

[13] C. Sinthanayothin, J. F. Boyce, H. L. Cook, T. H. Williamson, Automated localisation of the optic disc, fovea, and retinal blood vessels from digital colour fundus images, British Journal of Ophthalmology 83 (1999) 902–910.

[14] E. Ricci, R. Perfetti, Retinal blood vessel segmentation using line operators and support vector classification, Medical Imaging, IEEE Transactions on 26 (10) (2007) 1357–1365.

[15] D. Marín, A. Aquino, M. E. Gegúndez-Arias, J. M. Bravo, A new supervised method for blood vessel segmentation in retinal images by using gray-level and moment invariants-based features, Medical Imaging, IEEE Transactions on 30 (1) (2011) 146–158.

[16] G. B. Kande, P. V. Subbaiah, T. S. Savithri, Unsupervised fuzzy based vessel segmentation in pathological digital fundus images, Journal of medical systems 34 (5) (2010) 849–858.

[17] F. Zana, J. C. Klein, Segmentation of vessel-like patterns using mathematical morphology and curvature evaluation, IEEE Transactions on Image Processing 10 (2001) 1010–1019.

[18] A. Mendonça, A. Campilho, Segmentation of retinal blood vessels by combining the detection of centerlines and morphological reconstruction, Medical Imaging, IEEE Transactions on 25 (9) (2006) 1200–1213.

[19] K. Sun, Z. Chen, S. Jiang, Y. Wang, Morphological multiscale enhancement, fuzzy filter and watershed for vascular tree extraction in angiogram, Journal of medical systems 35 (5) (2011) 811–824.

[20] L. Chen, Y. Ju, S. Ding, X. Liu, Topological vascular tree segmentation for retinal images using shortest path connection, in: Image Processing (ICIP), 2011 18th IEEE International Conference on, 2011, pp. 2137–2140.

[21] M. Sofka, C. Stewart, Retinal vessel centerline extraction using multiscale matched filters, confidence and edge measures, Medical Imaging, IEEE Transactions on 25 (2006) 1531–1546.

[22] C. Wu, J. Kang Derwent, P. Stanchev, Retinal vessel radius estimation and a vessel center line segmentation method based on ridge descriptors, Journal of Signal Processing Systems 55 (1-3) (2009) 91–102.

[23] T. Walter, J. Klein, A computational approach to diagnosis of diabetic retinopathy, in: 6th Conference on Systemics, Cybernetics and Informatics (SCI), 2002, pp. 521–526.

[24] A. Bessaid, A. Feroui, M. Messadi, Detection of blood vessels from retinal images using watershed transformation, Journal of Mechanics in Medicine and Biology 09 (04) (2009) 633–642.

[25] J. Staal, M. Abramoff, M. Niemeijer, M. Viergever, B. van Ginneken, Ridge-based vessel segmentation in color images of the retina, Medical Imaging, IEEE Transactions on 23 (4) (2004) 501 –509.

[26] M. Ortega, M. Penedo, J. Rouco, N. Barreira, M. Carreira, Personal verification based on extraction and characterisation of retinal feature points, Journal of Visual Languages and Computing 20 (2) (2009) 80 – 90.

[27] P. Soille, Morphological Image Analysis: Principles and Applications, 2nd Edition, Springer-Verlag New York, Inc., 2003.

[28] S. Beucher, F. Meyer, The Morphological Approach to Segmentation : The Watershed Transformation, E. Dougherty Ed., 1992, Ch. 12, pp. 433–481.

[29] J. Angulo, D. Jeulin, Stochastic watershed segmentation, in: Proc. of the 8th International Symposium on MathematicalMorphology (ISMM'2007), 2007, pp. 265–279.

[30] R. O. Duda, P. E. Hart, Pattern Classification and Scene Analysis, John Wiley & Sons Inc, 1973.

[31] R. C. Gonzalez, R. E. Woods, S. L. Eddins, Digital Image Processing using MATLAB, Pearson Prentice Hall, 2004.

[32] T. Walter, Application de la Morphologie Mathématique au diagnostic de la Rétinopathie Diabétique à partir d'images couleur, École Nationale Supérieure des Mines de Paris, 2003, Ch. 3, pp. 39–46.

[33] J. Angulo, R. Verdú-Monedero, J. Morales-Sánchez, Multiscale local multiple orientation estimation using Mathematical Morphology and B-spline interpolation, Proc. of 7th Int. Symposium on Image and Signal Processing and Analysis (ISPA) (2011) 575 – 578.

[34] R. Verdú-Monedero, J. Angulo, J. Serra, Anisotropic morphological filters with spatially-variant structuring elements based on image-dependent gradient fields, IEEE Trans. Image Processing 20 (1) (2011) 200–212.

[35] A. G. Legaz-Aparicio, R. Verdú-Monedero, J. Morales-Sánchez, J. Larrey-Ruiz, J. Angulo, Detection of retinal vessel bifurcations by means of multiple orientation estimation based on regularized morphological openings, in: XIII Mediterranean Conference on Medical and Biological Engineering and Computing 2013, Vol. 41 of IFMBE Proceedings, Springer International Publishing, 2014, pp. 317–320.